Alginate beads as a highly versatile test-sample for optoacoustic imaging

Juan Pablo Fuenzalida-Werner [a,b,1], Kanuj Mishra [a,1], Mariia Stankevych [a], Uwe Klemm [a], Vasilis Ntziachristos [a,c,d], Andre C. Stiel [a,*]

[a] *Institute of Biological and Medical Imaging (IBMI), Helmholtz Zentrum München, D-85764 Neuherberg, Germany*
[b] *Chair of Biogenic Functional Materials, Technical University of Munich, D-94315 Straubing, Germany*
[c] *Chair of Biological Imaging, Technische Universität München, D-81675 München, Germany*
[d] *Center for Translational Cancer Research (TranslaTUM), D-81675 München, Germany*

A B S T R A C T

Test-samples are necessary for the development of emerging imaging approaches such as optoacoustics (OA); these can be used to benchmark new labeling agents and instrumentation, or to characterize image analysis algorithms or the inversion required to form the three-dimensional reconstructions. Alginate beads (AlBes) loaded with labeled mammalian or bacterial cells provide a method of creating defined structures of controllable size and photophysical characteristics and are well-suited for both *in vitro* and *in vivo* use. Here we describe a simple and rapid method for efficient and reproducible production of AlBes with specific characteristics and show three example applications with multispectral OA tomography imaging. We show the advantage of AlBes for studying and eventually improving photo-switching OA imaging approaches. As highly defined, homogeneous, quasi point-like signal sources, AlBes might hold similar advantages for studying other agents, light-fluence models, or the impact of detection geometries on correct image formation in the near future.

1. Introduction

Multispectral Optoacoustic tomography (MSOT) is a rapidly evolving optoacoustics (OA) imaging modality, with an increasing number of breakthrough clinical applications [1,2] and use in biomedical research [3–5]. Most MSOT studies presently rely on endogenous hemoglobin as contrast, but emerging use of dyes, nanoparticles [6] or transgene contrast agents [7] is enabling further applications in biomedical or life-science imaging. New imaging modalities and new methods of contrast generation require reliable approaches for benchmarking and characterization of instruments, analysis methods and contrast agents. Current methods for this purpose include preparation of *in vitro* ("phantoms") or *in vivo* test-samples and are characterized by marked disadvantages which often prevent acquisition of reproducible and correct data. For example, subcutaneous matrigel™ implants with OA agents [8] suffer from high inhomogeneity in spatial distribution and concentration (Supplementary Fig. 1a), which obscures the correlation between the detected and real distribution. Tubing filled with agents *in vitro* [9] or in *ex vivo* mice [10] allows to control the amount of analyte, but for cells in solution show sedimentation effects (Supplementary

Fig. 1b), moreover, the resulting margins are not natural since there is no interaction between the tubing and the surrounding tissue (Supplementary Fig. 1c). Additionally, the *ex vivo* application in mice omits typical confounders like breathing or heart-beat motion, often resulting in inaccurate observations in assessing the performance of analysis approaches or agent characteristics. A similar limitation is true for complete tissue phantoms [8] whose homogeneous background signal significantly differs from the complexity of an *in vivo* situation.

To address the above limitations, we herein developed Alginate Beads (AlBes) as a test-sample for OA. AlBes are characterized by a highly defined size and shape, can be loaded with cells carrying agents of interest, and can be used as point sources in *in vitro* phantoms as well as injected subcutaneously or intratumorally *in vivo*. Alginate beads are non-toxic and already used for encapsulating mammalian or bacterial cells [11,12]. Such beads are generated when a drop of alginate solution comes in contact with a solution of calcium [11,13] and can be prepared by centrifugal force [14]. The homogeneity of bead size and loading is essential in their use as a test and benchmarking tool for imaging applications. To this end, we developed an efficient procedure to produce alginate beads of exceptional homogeneity and demonstrate this crucial

---

feature in a number of OA applications. Importantly, the production routine requires only readily available lab equipment (*i.e.* hanging-rotor centrifuge, falcon tubes, syringes, and needles), thus enabling a widespread applicability towards advancing OA.

2. Results & discussion

2.1. Alginate bead preparation

We developed a 3D printed cap for standard disposable 50 mL conical tubes. (Fig. 1a, printer-file obtainable with the extended material). This cap fits a one milliliter syringe positioned in the center of the falcon tube (Fig. 1b). In this configuration, the alginate solution drips from the syringe and, upon making contact with the calcium solution acting as a reservoir in the tube, jellifies to form beads. The choice of needle gauges allows precise control over the AlBes size. The full step-by-step procedure can be found in the extended materials (Supplementary info 1).

2.2. Characterization

To demonstrate the uniformity in size, shape and loading of AlBes, we prepared beads with a 30 G needle loaded with bacteria expressing the photo-switchable label *Re*BphP-PCM [15] absorbing in the near-infrared (NIR). We imaged 150 beads with a fluorescence microscope using the Cy5.5 filter and determined their size and homogeneity. As shown in Fig. 1c, all beads are round and show homogenous fluorescence. The average size was 456 ± 2 μm, while a size distribution frequency analysis gave a size of 459 ± 2 μm (Fig. 1d); both measurements indicate that our methodology produced highly homogeneous beads in size. Next, we measured how the fluorescence signal distributed inside and among the beads. As Fig. 1e shows, the fluorescence signal increases from the edges to the center in all the beads, due to the epifluorescence recording, with a standard deviation of only 3.5 % among the beads. Therefore, bacteria are equally distributed within the beads, and all produced beads share the same distribution and overall loading of bacteria. To show full control of the concentration of cells loaded to the beads we prepared beads with different concentrations of bacteria

expressing the photo-switchable label *Re*BphP-PCM. Measurements of the bacterial solutions before bead preparation and the respective beads show a high linearity (Supplementary Fig. 2). This suggests that the preparation of AlBes with an exactly defined loading of cells is possible and that the loading of the beads is directly related to the signal of the loaded beads. For experimental convenience, we tested the optimal storage conditions after bead preparation. The beads were stable in size and fluorescence at 4 °C in milliQ water and without any solvent over 24 h, 48 h and 72 h (Table 1). Interestingly, when using several different buffer systems (PBS, HEPES, MOPS, HBSS) the beads slightly increased in size and showed up to 40 % loss in fluorescence (Supplementary Table 1). However, this loss is once and afterwards the size and signal stay stable, likely due the chelation of calcium ions inside the beads by the ions of the buffer systems. Similar to bacteria AlBes can be also loaded with mammalian cells, exemplified by beads loaded with HCT116 cells expressing *Re*BphP-PCM and GFP. Similarly, to the bacteria there is a clear linear relationship between the cell number in solution and the fluorescence signal of the formed beads Supplementary Fig. 3.

In order to benchmark instrument and algorithm performance it is essential to generate test-samples of defined size, *e.g.* to determine resolution. The size of alginate beads can be controlled by different methods such as centrifugal speed, alginate concentration, or by the

Table 1

Bead stability based on size **(a)** and fluorescence **(b)**. Shown is the mean and standard deviation normalized for 0 h(n = 20). See also Supplementary Table 1.

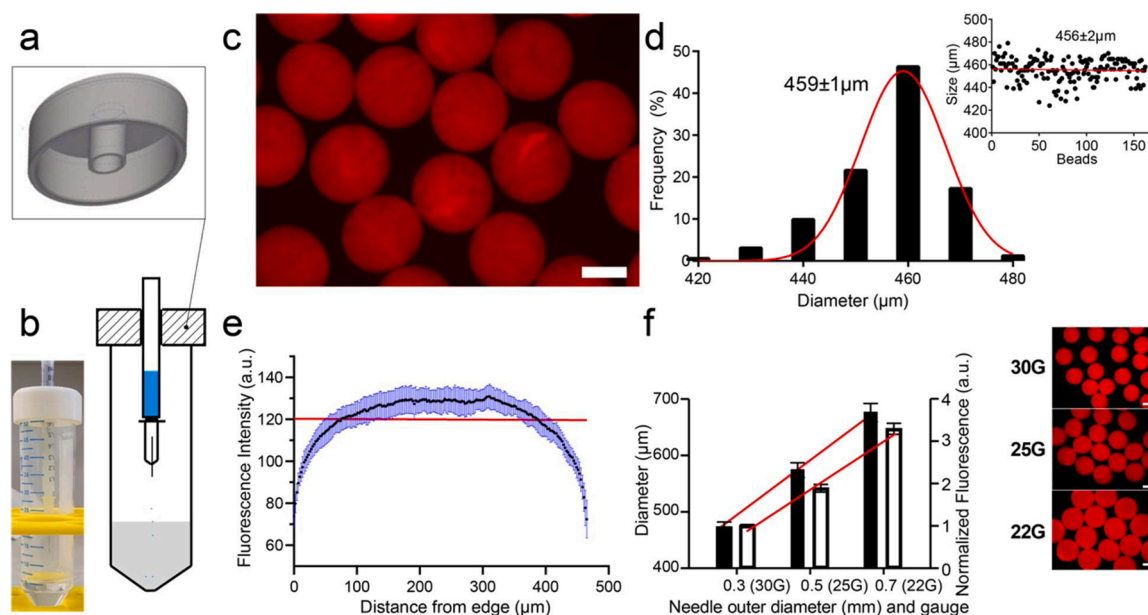| a	after x h in	Water		
	0	1,00	±	0,01
	24	1,00	±	0,01
	48	1,00	±	0,02
	72	1,00	±	0,02
b	after x h in	Water		
	0	1,00	±	0,04
	24	1,03	±	0,11
	48	1,01	±	0,05
	72	1,02	±	0,04

Fig. 1. **a)** 3D design of a falcon cap for bead production. **b)** Titration concept. The alginate solution is shown in blue, and the calcium solution is shown in gray. **c)** Fluorescence microscopy picture of 30 G beads loaded with *E. coli* expressing *Re*BphP-PCM. Scale bar 250 μm. **d)** 30 G beads diameter distribution with Gaussian fit probability density, with the insert showing an arithmetic average (n = 162). **e)** 30 G bead fluorescence intensity profile (n = 162). **f)** Bead average diameter and normalized sum fluorescence intensity prepared by different gauge needles, with the insert showing a microscopy picture of the same beads (n = 12 per sample).

addition of surfactants [14,16]. These approaches introduce several variables resulting in confounders such as high alginate concentrations yielding preparation artefacts. In OA, a change in alginate concentration can change the sound propagation parameters (Grüneisen) and surfactants can influence the comparability of signals. We therefore controlled AlBes size *via* the highly standardized and easily interchangeable commercial needle gauge. Importantly, in contrast to surfactant or alginate concentration methods, the size control *via* the gauge keeps the overall bead composition constant (alginate and agent concentration), allowing to produce beads with similar characteristics but of different size. The AlBes produced with our method using different needle gauges showed a clear linear relation between needle size diameter and the size of the generated beads (Fig. 1f). To ensure that the procedure does not affect agent loading (fluorescent bacteria), we measured the fluorescence signal of the different bead sizes. The sum fluorescence intensity increased with the bead size (Fig. 1f), but normalizing the values to bead volume resulted in similar intensities (~1), confirming similar bacterial loading.

We next investigated the properties of the beads using a commercial multispectral optoacoustic tomography (MSOT) device. We probed the signal of beads loaded with the transgene label *Re*BphP-PCM at 770 nm (Fig. 2a). Interestingly, the size of the beads for all three tested gauge sizes was consistently ~5% smaller when assessed by MSOT than when assessed by light microscopy (Table 2). The size of AlBes produced with the 22 G needle is near the physical resolution of the MSOT device. These AlBes thus constitute a perfect voxel-sized point source in our MSOT device, ideal for measurement, reconstruction and analysis characterization.

Next, we show three AlBes applications: i) instrument assessment, ii) unmixing algorithm assessment and iii) label performance comparison.

2.3. Instrument characteristics

The defined shape and margins of AlBes allow us to map the light fluency inside a phantom and the detection sensitivity of MSOT's transducer array. Due to the absorptive and scattering characteristics, light fluence is reduced towards the center of the phantom as can be seen from the reduced intensity of the OA signal of uniform AlBes towards the phantoms' center (Fig. 2b). The individual intensity fluctuation can stem from the placement of the beads not being perfectly aligned (Fig. 2a) or from the influence of single detector elements on the overall signal. We employed established commercial reconstruction algorithms, however AlBes might also be particular useful to advance reconstruction approaches [17] including as point source to study and overcome ring-artifacts and sidelobes [18].

2.4. Comparing temporal unmixing strategies

The transgene label that we used for testing purposes, *Re*BphP-PCM, belongs to a novel class of reversibly switchable proteins for

Table 2
Beads radius comparison between MSOT and light microscopy (n = 12).

	Radius (µm)		
Needle Size	30 G, 0.3 mm	25 G, 0.5 mm	22 G, 0.7 mm
Microscope	237 ± 9	287 ± 13	338 ± 16
MSOT	220 ± 14	272 ± 21	320 ± 21

optoacoustics (rsOAPs). These labels can be photo-switched by light between an ON and OFF state allowing a modulation that can be used to separate the signal of *Re*BphP-PCM labeled cells from the background (*e. g.* blood hemoglobin). Transgene rsOAPs are advocated by us [15] and others [5,19,20] as a unique way to overcome the contrast limitations of OA and allow the detection of small cell numbers deep in the tissue/animal. Analysis of this modulation data requires analysis of the temporal behavior of the contrast in the images in correlation to the employed switching light [15]. Thus, in contrast to conventional transgene labels that can be used in OA like iRFP720 [21] which are unmixed using their spectral signatures the unmixing of rsOAPs uses a temporal signature unique to the label. We showcase this difference in a phantom experiment with both proteins (Supplemental Fig. 4).

For temporal unmixing different strategies can be used here we exemplarily use AlBes as a defined ground-truth for algorithm benchmarking *in vivo*. Although we regularly use histology to confirm the ground-truth, the use of AlBes has the advantage that the exact margins of the signal source are exceptionally well-suited to assess fundamental phenomena of the algorithms, like clear spatially accurate unmixing. Like other rsOAPs stemming from BphP, *Re*BphP-PCM photo-switches by alternating illumination in the NIR. In our MSOT measurements the modulation is achieved by repeatedly illuminating the sample with 680 nm and 770 nm pulses of light. We performed *in vivo* experiments by injecting one single bead containing bacterial cells expressing *Re*BphP-PCM inside a xenograft breast tumor model (4T1). We compared the performance of four different approaches to extract the photo-modulation patterns and identify (unmix) positions in the images that can stem from the AlBes loaded with rsOAP expressing bacteria (for details on the approaches see Material & Methods and supplementary info 2), with one approach being the machine learning based analysis we have previously reported [15]. The results were compared against histology, showing a perfect round bead as the ground truth (Fig. 3e and Supplemental Fig. 5). All temporal unmixing strategies were able to detect some of the pixels of the bead (Fig. 3a–d and f). However, they differed significantly in the correlation between true and predicted values, Matthews correlation coefficient, and especially in the number of false positives (Fig. 3f and Supplemental Fig. 5g).

2.5. Comparing label performance

A particularly well-suited application of AlBes is the comparison of different labeling agents under standardized conditions *in vivo*. In
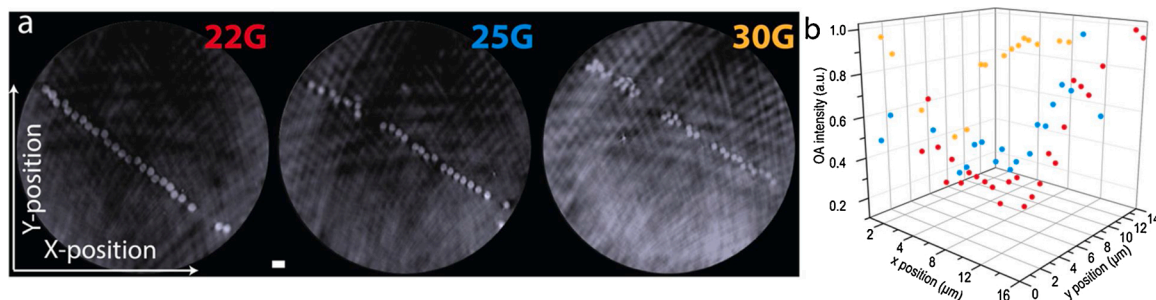

Fig. 2. a) Optoacoustic tomography test on alginate beads loaded with *E. coli* expressing *Re*BphP-PCM, **b)** Optoacoustic signal intensity dependency on location of the beads in the field of view due to inhomogeneous switching-on light field. Note the changes of size of the beads indicated in black (22 G needle produced), blue (25 G), and red (30 G). Scale bars 1000 µm.
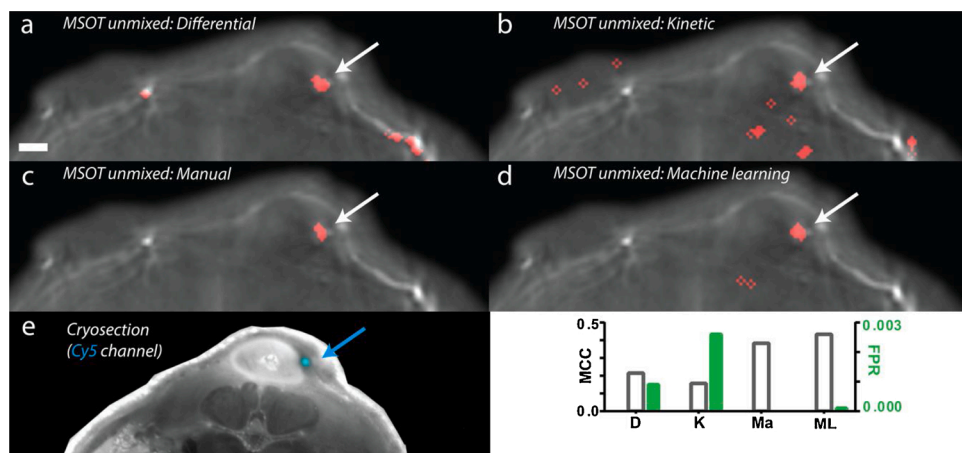
Fig. 3. MSOT images of a 4T1 tumor model injected with a bead loaded with *E. coli* expressing photo-switching *Re*BphP-PCM (arrow). Further signals are false positives **a-d)** Unmixing based on the photo-switching characteristics was conducted with four different algorithms. **e)** Ground truth based on fluorescence imaging (Cy 5.5 channel) of cryosections of the relative area depicted in MSOT a-d. Scale bar 1 mm. Further examples of *in vivo* application of AlBes can be found in Suppl. Fig. 5. **f)** Accuracy of photo-switching based unmixing as Matthews correlation coefficient (MCC) and false positive rate (FPR), see also Suppl. Fig. 5g.

regards to photo-switching labels, an additional design goal for the development of novel labels is to enable photo-switching signatures that can be differentiated from other rsOAPs to allow multiplexing. *In vitro* results showed that two rsOAPs, *Dr*BphP-PCM and *Re*BphP-PCM, have different relaxation kinetics while being illuminated with 770 nm light, (Supplementary Fig. 6). However, when we compared beads containing bacteria expressing the two labels injected individually into a 4T1 tumor model, we saw a clear difference in the observed relaxation time between *in vitro* and *in vivo* (Fig. 4). A primary reason can be light fluence or differences in the relaxation time of the reconstructed / unmixed data *versus* the direct observation *in vitro*. While the difference was still pronounced enough to be recognized by the algorithm as two different labels, this example demonstrates that a controlled *in vivo* comparison, such as with AlBes, is essential and might not necessarily reflect the *in vitro* results.

3. Summary

Our data shows the ease of production, reproducibility, precision and applicability of AlBes and their use as highly defined test-samples which we exploited for OA imaging. We could show that test-sample objects with clear margins can be indispensable tools in developing and calibrating labels as well as imaging instrumentation and algorithms either *in vitro* or *in vivo*, with the latter particularly critical since defined *in vivo* models are essential for the development of advanced labels and imaging concepts. This includes rsOAP imaging, since photophysical, quantification and unmixing properties are often profoundly affected by light fluence [22], whose natural heterogeneity can only be adequately represented in *in vivo* samples. Beyond our examples using AlBes loaded

with label expressing bacteria, such beads can also be prepared with mammalian cells [11,12] and possibly with pure dye or protein loading using polymers as coadjutants to improve dye retention [23].

4. Material and methods

4.1. Material

Alginic acid sodium salt, calcium chloride and chemical reagent for buffer preparation were purchased from Sigma-Aldrich.

4.2. E. coli expressing rsOAPs

rsOAPs (*Dr*BphP-PCM or *Re*BphP-PCM) have been expressed in *Escherichia coli* strain BL21 (DE3) (New England Biolabs, #C2527). In brief, plasmids expressing rsOAPs and HO were transformed into the BL21 host cells. Bacterial cells were grown in LB media supplemented with ampicillin at 37 °C until the culture reached an OD (optical density) of 0.6, followed by induction of protein expression by addition of IPTG (isopropyl-β-D-thiogalactopyranoside) and further incubation for 16–18 h at 22 °C.

4.3. Beads & phantom preparation

A 2% solution of sodium alginate was prepared in water. *E. coli* strain BL21 cells expressing *Dr*BphP-PCM or *Re*BphP-PCM were harvested by centrifugation and then mixed with the alginate solution. Beads were formed by filling the alginate cell mixtures in the syringe with different needle sizes, followed by centrifugation (300 rpm), which allowed the
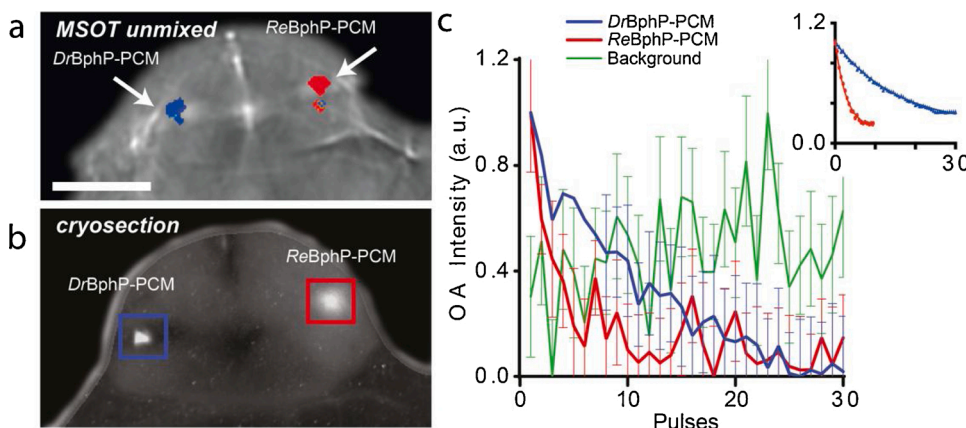

Fig. 4. *In vivo* imaging of alginate beads containing *E. coli* expressing rsOAPs *Re*BphP-PCM and DrBphP-PCM, respectively. **a)** Unmixed OA image showing two rsOAPs (blue, *Dr*BphP-PCM and red, *Re*BphP-PCM). **b)** Ground truth based on fluorescence imaging (Cy 5.5 channel) of cryosections of the relative area depicted in MSOT a. Scale bar 1 mm. **c)** Mean of switching kinetics over the measurement for the two types of beads shown together with the background. **Inset:** Switching cycles of pure protein *Dr*BphP-PCM and *Re*BphP-PCM. Crosswise correlation between *in vivo* and pure protein yields the assignment: for *Re*BphP-PCM the correlation to the pure-protein reference is 0.945 (0.804 for the *Dr*BphP-PCM reference) while for *Dr*BphP-PCM the correlation is 0.988 (0.907 for the *Re*BphP-PCM reference), see also Suppl. Fig. 6.

dropwise addition of the mixtures into $CaCl_2$ (200 mM). The beads were allowed to solidify before $CaCl_2$ was replaced by fresh distilled water. Agar phantom were prepared by distributing the bead in an agar / intralipid emulsion. Phantoms were subsequently imaged by MSOT as described elsewhere [15].

4.4. Mouse work

All animal experiments were approved by the government of Upper Bavaria and were carried out in accordance with the approved guidelines. For mouse injection, beads containing *Dr*BphP-PCM or *Re*BphP-PCM were selected under light microscopy and *intratumorally* injected into mouse bearing xenograph 4T1 tumor using a 30 G gauge Hamilton syringe.

4.5. MSOT setup and data acquisition

Phantom and mice data were acquired using a commercially available MSOT scanner (MSOT In Vision 256-TF, iThera Medical GmbH, Munich, Germany). The acquired acoustic data were reconstructed using the ViewMSOT version 3.8.1.04 (iThera Medical GmbH, Munich, Germany)

4.6. Temporal unmixing strategies

All unmixing strategies used data reconstructed with ViewMSOT (iThera) using backprojection reconstruction. For all analysis an initial movement correction using phase-based and non-rigid spline-based methods was conducted. **Differential method:** Mean of all cycles. The minimum value was subtracted from maximum value of the mean cycle. Limits for segmentation were set to obtain optimal results, *i.e.* maximum true positives (TPR) and minimum false positives (FPR). **Kinetic method:** Mean of all cycles. The coefficient for the exponential fit (exp (-b(x+1)) on a mean cycle was obtained. Limits for segmentation were set to obtain optimal results, *i.e.* maximum true positives (TPR) and minimum false positives (FPR). **Manual method:** A set of features was chose as described in Mishra et al. [15] (The features are: i-ii) the coefficient for the exponential fit (exp(b(x+1)) and -exp(b(x-1)+1) of the mean kinetic (mean of all cycles), iii) R [2] of the fit, iv) the mean intensity over the signal, v) amplitude (max-min) of all the signal, viix) median maximums and minimums of cycles along with standard deviation, x) number of cycles with increasing or decreasing trend, xi) the length of the part of the cycle that shows a trend, *i.e.* at what point the signal vanishes in the noise, and xii) Fourier coefficient for the expected frequency defined by the photo-control schedule.). Limits for all features were chosen manually for segmentation to obtain optimal results, *i.e.* maximum true positives (TPR) and minimum false positives (FPR). **Machine learning method:** Similar features as for the manual methods were calculated. The features were analyzed by a pretrained model based on random forest of decisions trees. Training and validation datasets for the model were built from datasets of FoxN1 mice bearing 4T1 tumors measured on day 9 and FoxN1 mice with *sub cutaneous* Jurkat T lymphocytes injections (8000 cells/μl). This training data was taken from Mishra et al. [15].

Author contributions

J.P.F.-W. and K.M. performed all measurements and analyzed the *in vitro* data. M.S. performed data analysis of photo-switching data. U.K. assisted for *in vivo* measurements. V.N. contributed to the manuscript. J. P.F.-W. and A.C.S. designed the study and wrote the manuscript.

Raw data availability statement

All raw data except OA tomography data is available from zenodo. org under the indetifier: https://doi.org/10.5281/zenodo.5499956. OA tomography data is available from the authors upon request.

Declaration of Competing Interest

V.N. is a shareholder of iThera Medical GmbH. The authors declare that there are no further conflicts of interest.

Appendix A. Supplementary data

Supplementary material related to this article can be found, in the online version, at doi:https://doi.org/10.1016/j.pacs.2021.100301.

References

[1] F. Knieling, et al., Multispectral optoacoustic tomography for assessment of Crohn's disease activity, N. Engl. J. Med. 376 (2017) 1292–1294.

[2] A.P. Regensburger, et al., Detection of collagens by multispectral optoacoustic tomography as an imaging biomarker for Duchenne muscular dystrophy, Nat. Med. 25 (2019) 1905–1915.

[3] J. Reber, M. Willershäuser, A. Karlas, K. Paul-Yuan, G. Diot, D. Franz, T. Fromme, S.V. Ovsepian, N. Bézière, E. Dubikovskaya, D.C. Karampinos, C. Holzapfel, H. Hauner, M. Klingenspor, V. Ntziachristos, Non-invasive measurement of brown fat metabolism based on optoacoustic imaging of hemoglobin gradients, Cell Metab. 27 (2018) 689–701, e4.

[4] J. Wang, A.S. Jeevarathinam, K. Humphries, A. Jhunjhunwala, F. Chen, A. Hariri, B.R. Miller, J.V. Jokerst, A mechanistic investigation of methylene blue and heparin interactions and their photoacoustic enhancement, Bioconjug. Chem. 29 (2018) 3768–3775.

[5] J. Märk, H. Dortay, A. Wagener, E. Zhang, J. Buchmann, C. Grötzinger, T. Friedrich, J. Laufer, Dual-wavelength 3D photoacoustic imaging of mammalian cells using a photoswitchable phytochrome reporter protein, Commun. Phys. 1 (2018) 3, https://doi.org/10.1038/s42005-017-0003-2.

[6] V. Gujrati, A. Mishra, V. Ntziachristos, Molecular imaging probes for multi-spectral optoacoustic tomography, Chem. Commun. 53 (2017) 4653–4672.

[7] J. Brunker, J. Yao, J. Laufer, S.E. Bohndiek, Photoacoustic imaging using genetically encoded reporters: a review, J. Biomed. Opt. 22 (2017) 70901.

[8] J.P.J.P. Fuenzalida Werner, K. Mishra, Y. Huang, P. Vetschera, S. Glasl, A. Chmyrov, K. Richter, V. Ntziachristos, A.C. Stiel, Structure-based mutagenesis of phycobiliprotein smURFP for optoacoustic imaging, ACS Chem. Biol. 14 (2019) 1896–1903.

[9] A.C. Stiel, X.L. Deán-Ben, Y. Jiang, V. Ntziachristos, D. Razansky, G.G. Westmeyer, High-contrast imaging of reversibly switchable fluorescent proteins via temporally unmixed multispectral optoacoustic tomography, Opt. Lett. 40 (2015) 367.

[10] S. Tzoumas, A. Nunes, I. Olefir, S. Stangl, P. Symvoulidis, S. Glasl, C. Bayer, G. Multhoff, V. Ntziachristos, Eigenspectra optoacoustic tomography achieves quantitative blood oxygenation imaging deep in tissues, Nat. Commun. 7 (2016) 12121.

[11] M. Kierstan, C. Bucke, The immobilization of microbial cells, subcellular organelles, and enzymes in calcium alginate gels, Biotechnol. Bioeng. 19 (3) (1977) 387–397, https://doi.org/10.1002/bit.260190309.

[12] G. Orive, A.M. Carcaboso, R.M. Hernández, A.R. Gascón, J.L. Pedraz, Biocompatibility evaluation of different alginates and alginate-based microcapsules, Biomacromolecules 6 (2) (2005) 927–931, https://doi.org/10.1021/bm049380x.

[13] T.A. Read, D.R. Sorensen, R. Mahesparan, P. Enger, R. Timpl, B.R. Olsen, M.H. B. Hjelstuen, O. Haraldseth, R. Bjerkvig, Local endostatin treatment of gliomas administered by microencapsulated producer cells, Nat. Biotechnol. 19 (1) (2001) 29–34, https://doi.org/10.1038/83471.

[14] H.B. Eral, E.R. Safai, B. Keshavarz, J.J. Kim, J. Lee, P.S. Doyle, Governing principles of alginate microparticle synthesis with centrifugal forces, Langmuir 32 (2016) 7198–7209.

[15] K. Mishra, M. Stankevych, J.P. Fuenzalida Werner, S. Grassmann, V. Gujrati, U. Klemm, V.R. Buchholz, V. Ntziachristos, A.C. Stiel, Multiplexed whole animal imaging with reversibly switchable optoacoustic proteins, Sci. Adv. 6 (2020) eaaz6293.

[16] F. Davarci, D. Turan, B. Ozcelik, D. Poncelet, The influence of solution viscosities and surface tension on calcium-alginate microbead formation using dripping

technique, Food Hydrocolloids 62 (2017) 119–127, https://doi.org/10.1016/j.foodhyd.2016.06.029.

[17] C. Lutzweiler, D. Razansky, Optoacoustic imaging and tomography: reconstruction approaches and outstanding challenges in image performance and quantification, Sensors (Switzerland) 13 (2013) 7345–7384.

[18] M. Mozaffarzadeh, A. Hariri, C. Moore, J.V. Jokerst, The double-stage delay-multiply-and-sum image reconstruction method improves imaging quality in a LED-based photoacoustic array scanner, Photoacoustics 12 (2018) 22–29.

[19] L. Li, A.A. Shemetov, M. Baloban, P. Hu, L. Zhu, D.M. Shcherbakova, R. Zhang, J. Shi, J. Yao, L.V. Wang, V.V. Verkhusha, Small near-infrared photochromic protein for photoacoustic multi-contrast imaging and detection of protein interactions in vivo, Nat. Commun. 9 (2018) 2734.

[20] R.K.W. Chee, Y. Li, W. Zhang, R.E. Campbell, R.J. Zemp, In vivo photoacoustic difference-spectra imaging of bacteria using photoswitchable chromoproteins, J. Biomed. Opt. 23 (2018) 1.

[21] D.M. Shcherbakova, V.V. Verkhusha, Near-infrared fluorescent proteins for multicolor in vivo imaging, Nat. Methods 10 (2013) 751–754.

[22] P. Vetschera, K. Mishra, J.P. Fuenzalida-Werner, A. Chmyrov, V. Ntziachristos, A. C. Stiel, Characterization of reversibly switchable fluorescent proteins in optoacoustic imaging, Anal. Chem. 90 (2018) 10527–10535.

[23] E. Araya-Hermosilla, D. Muñoz, S. Orellana, A. Yáñez, A.F. Olea, F. Oyarzun-Ampuero, I. Moreno-Villoslada, Immobilization of rhodamine 6G in calcium alginate microcapsules based on aromatic-aromatic interactions with poly(sodium 4-styrenesulfonate), React. Funct. Polym. 81 (1) (2014) 14–21, https://doi.org/10.1016/j.reactfunctpolym.2014.03.017.

Kanuj Mishra received his Diploma in Medical Biotechnology from the All India Institute of Medical Sciences (AIIMS), New Delhi, India. After a short stay at the Department for Neuro-anatomy at the University of Saarland, Homburg, Germany he joined the Cell Engineering Group at the Institute for Biological and Medical Imaging (IBMI) at the Hemholtz Zentrum München, Germany, in 2017 as PhD student.

Dr. rer. nat. Juan-Pablo Fuenzalida Werner studied pharmaceutical chemistry at the Universidad Austral de Chile (Chile). In 2015, he got his PhD in Biology from the University of Münster (Germany), studying the interaction between polysaccharides and proteins under Prof. Dr. Francisco Goycoolea. In 2016, he started as a postdoctoral researcher in the Cell Engineering group of Dr. Andre Stiel at IBMI at the Helmholtz Zentrum München (Germany), working on the development and understanding of new genetically encoded labels as well as new optoacoustic instrumentation. Since September 2020, he has been a subgroup leader /akademischer rat working on developing optoelectronic proteins at the chair of biogenic functional materials led by Prof. Dr. Rubén D. Costa at the Technical University of München.

Andre C. Stiel. After receiving his Diploma in Biology from the Ruhr University Bochum in the Department of Biophysics (Klaus Gerwert), ACS conducted his Ph.D. studies at the Max Planck Institute for Biophysical Chemistry, Göttingen, in the group of Nobel Laureate Stefan Hell where he was pivotal in pioneering the field of photo-switchable proteins for super-resolution imaging. After receiving his Ph.D. from the Ruprecht-Karls University, Heidelberg, in 2008 ACS moved for a postdoctoral stay to the Max Planck Institute for Developmental Biology, Tübingen, where he worked on computer aided protein engineering in the group of Birte Höcker, specifically pioneering a sensor for direct visualization of auxin which created significant attention. During his time in Tübingen ACS spend time as a guest researcher at the HHMI research campus Janelia Farm. In 2015 ACS moved to Munich to start the CellEngineering group at the Institute for Biological and Medical Imaging headed by Vasilis Ntziachristos a world leading researcher in the field of Optoacoustics. Since then ACS is key to advancing the field of genetically encoded Optoacoustic contrast agents. He also picked up on his favorite topic of photo-switchable proteins, by introducing (in parallel with an US consortium) photo-switching as a unique way to overcome background limitations in Optoacoustic imaging and enable the method for the visualization of small cell numbers deep in the animal.